Multi-Body Model - Micro Station

Dehaeze Thomas

November 18, 2024

Contents

From the start of this work, it became increasingly clear that an accurate micro-station model was necessary.

First, during the uniaxial study, it became clear that the micro-station dynamics affects the nano-hexapod dynamics. Then, using the 3-DoF rotating model, it was discovered that the rotation of the nano-hexapod induces gyroscopic effects that affect the system dynamics and should therefore be modeled. Finally, a modal analysis of the micro-station showed how complex the dynamics of the station is. The modal analysis also confirm that each stage behaves as a rigid body in the frequency range of interest. Therefore, a multi-body model is a good candidate to accurately represent the micro-station dynamics.

In this report, the development of such a multi-body model is presented.

First, each stage of the micro-station is described. The kinematics of the micro-station (i.e. how the motion of the stages are combined) is presented in Section 1.

Then, the multi-body model is presented and tuned to match the measured dynamics of the micro-station (Section 2).

Disturbances affecting the positioning accuracy also need to be modeled properly. To do so, the effects of these disturbances were first measured experimental and then injected into the multi-body model (Section 3).

To validate the accuracy of the micro-station model, "real world" experiments are simulated and compared with measurements in Section 4.

1 Micro-Station Kinematics

The micro-station consists of 4 stacked positioning stages (Figure 1.1). From bottom to top, the stacked stages are the translation stage D_y, the tilt stage R_y, the rotation stage (Spindle) R_z and the positioning hexapod. Such a stacked architecture allows high mobility, but the overall stiffness is reduced, and the dynamics is very complex. complex dynamics.
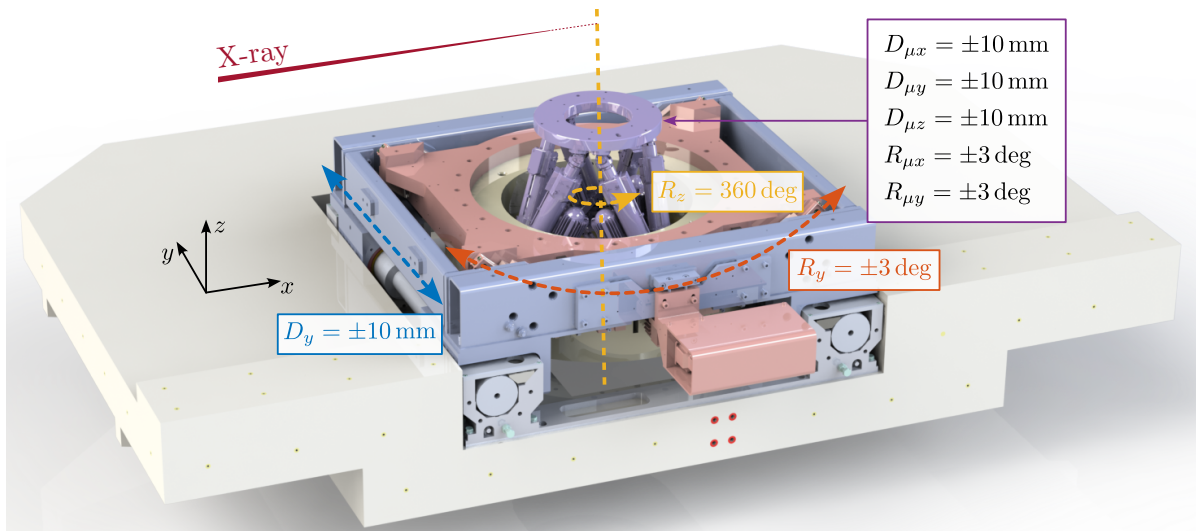

Figure 1.1: CAD view of the micro-station with the translation stage (in blue), tilt stage (in red), rotation stage (in yellow) and positioning hexapod (in purple). On top of these four stages, a solid part (shown in green) will be replaced by the stabilization stage.

There are different ways of modeling the stage dynamics in a multi-body model. The one chosen in this work consists of modeling each stage by two solid bodies connected by one 6-DoF joint. The stiffness and damping properties of the joint s can be tuned separately for each DoF.

The "controlled" DoF of each stage (for instance the D_y direction for the translation stage) is modeled as infinitely rigid (i.e. its motion is imposed by a "setpoint") while the other DoFs have limited stiffness to model the different micro-station modes.

1.1 Motion Stages

Translation Stage   The translation stage is used to position and scan the sample laterally with respect to the X-ray beam.

A linear motor was first used to enable fast and accurate scans. It was later replaced with a stepper

motor and lead-screw, as the feedback control used for the linear motor was unreliable[1]. An optical linear encoder is used to measure the stage motion and for controlling the position.

Four cylindrical bearings[2] are used to guide the motion (i.e. minimize the parasitic motions) and have high stiffness.

Tilt Stage   The tilt stage is guided by four linear motion guides[3] which are placed such that the center of rotation coincide with the X-ray beam. Each linear guide is very stiff in radial directions such that the only DoF with low stiffness is in R_y.

This stage is mainly used in *reflectivity* experiments where the sample R_y angle is scanned. This stage can also be used to tilt the rotation axis of the Spindle.

To precisely control the R_y angle, a stepper motor and two optical encoders are used in a PID feedback loop.
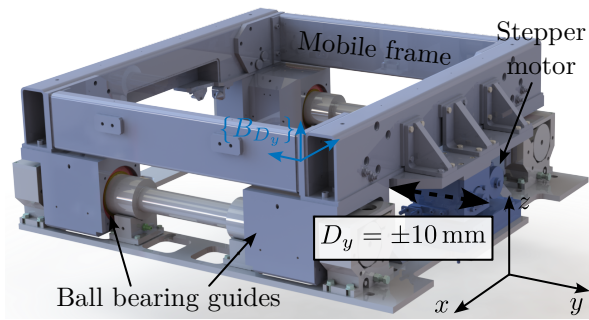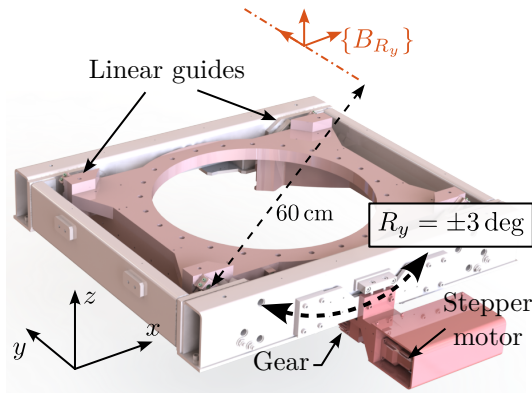

Figure 1.2: Translation Stage

Figure 1.3: Tilt Stage

Spindle   Then, a rotation stage is used for tomography experiments. It is composed of an air bearing spindle[4], whose angular position is controlled with a 3 phase synchronous motor based on the reading of 4 optical encoders.

Additional rotary unions and slip-rings are used to be able to pass electrical signals, fluids and gazes through the rotation stage.

Micro-Hexapod   Finally, a Stewart platform[5] is used to position the sample. It includes a DC motor and an optical linear encoders in each of the six struts.

This stage is used to position the point of interest of the sample with respect to the spindle rotation axis. It can also be used to precisely position the PoI vertically with respect to the x-ray.

---

[1]It was probably caused by rust of the linear guides along its stroke.
[2]Ball cage (N501) and guide bush (N550) from Mahr are used.
[3]HCR 35 A C1, from THK.
[4]Made by LAB Motion Systems.
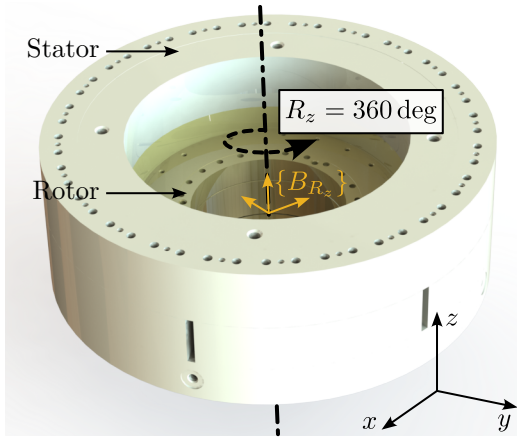[5]Modified Zonda Hexapod by Symetrie.
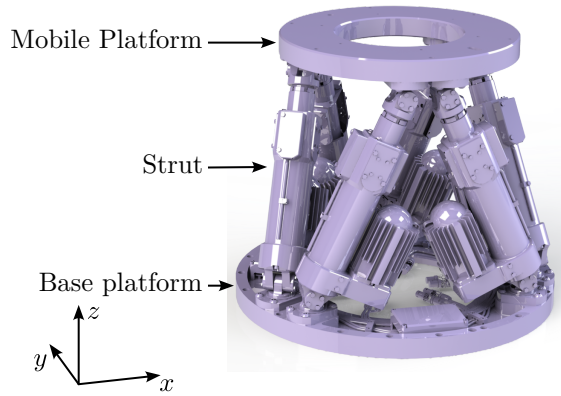
Figure 1.4: Rotation Stage (Spindle)

Figure 1.5: Micro Hexapod

1.2 Mathematical description of a rigid body motion

In this section, mathematical tools[6] that are used to describe the motion of positioning stages are introduced.

First, the tools to describe the pose of a solid body (i.e. it's position and orientation) are introduced. The motion induced by a positioning stage is described by transformation matrices. Finally, the motions of all stacked stages are combined, and the sample's motion is computed from each stage motion.

Spatial motion representation   The *pose* of a solid body relative to a specific frame can be described by six independent parameters. Three parameters are typically used to describe its position, and three other parameters describe its orientation.

The *position* of a point P with respect to a frame $\{A\}$ can be described by a 3×1 position vector (1.1). The name of the frame is usually added as a leading superscript: ^{A}P which reads as vector P in frame $\{A\}$.

$$^{A}P = \begin{bmatrix} P_x \\ P_y \\ P_z \end{bmatrix} \tag{1.1}$$

A pure translation of a solid body (i.e., of a frame $\{B\}$ attached to the solid body) can be described by the position $^{A}P_{O_B}$ as shown in Figure 1.6a.

The *orientation* of a rigid body is the same at all its points (by definition). Hence, the orientation of a rigid body can be viewed as that of a moving frame attached to the rigid body. It can be represented in several different ways: the rotation matrix, the screw axis representation, and the Euler angles are common descriptions.

---

[6]The tools presented here are largely taken from [1].

6

(a) Pure translation   **(b)** Pure rotation   **(c)** General transformation
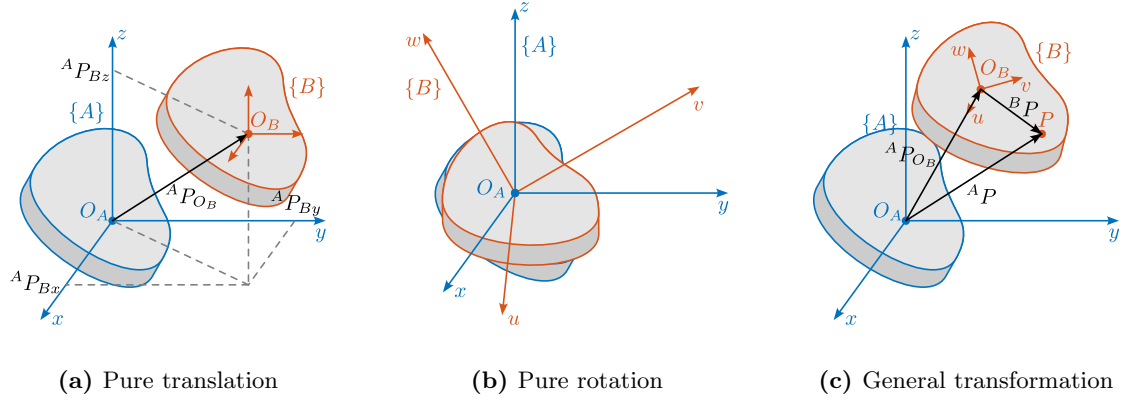
Figure 1.6: Rigid body motion representation. (a) pure translation. (b) pure rotation. (c) combined rotation and translation.

The rotation matrix $^A\boldsymbol{R}_B$ is a 3×3 matrix containing the Cartesian unit vectors of frame $\{\boldsymbol{B}\}$ represented in frame $\{\boldsymbol{A}\}$ (1.2).

$$^A\boldsymbol{R}_B = \begin{bmatrix} ^A\hat{\boldsymbol{x}}_B | ^A\hat{\boldsymbol{y}}_B | ^A\hat{\boldsymbol{z}}_B \end{bmatrix} = \begin{bmatrix} u_x & v_x & z_x \\ u_y & v_y & z_y \\ u_z & v_z & z_z \end{bmatrix} \tag{1.2}$$

Consider a pure rotation of a rigid body ($\{\boldsymbol{A}\}$ and $\{\boldsymbol{B}\}$ are coincident at their origins, as shown in Figure 1.6b). The rotation matrix can be used to express the coordinates of a point P in a fixed frame $\{A\}$ (i.e. ^AP) from its coordinate in the moving frame $\{B\}$ using Equation (1.3).

$$^AP = {}^A\boldsymbol{R}_B \, {}^BP \tag{1.3}$$

For rotations along x, y or z axis, the formulas of the corresponding rotation matrices are given in Equation (1.4).

$$\boldsymbol{R}_x(\theta_x) = \begin{bmatrix} 1 & 0 & 0 \\ 0 & \cos(\theta_x) & -\sin(\theta_x) \\ 0 & \sin(\theta_x) & \cos(\theta_x) \end{bmatrix} \tag{1.4a}$$

$$\boldsymbol{R}_y(\theta_y) = \begin{bmatrix} \cos(\theta_y) & 0 & \sin(\theta_y) \\ 0 & 1 & 0 \\ -\sin(\theta_y) & 0 & \cos(\theta_y) \end{bmatrix} \tag{1.4b}$$

$$\boldsymbol{R}_z(\theta_z) = \begin{bmatrix} \cos(\theta_z) & -\sin(\theta_z) & 0 \\ \sin(\theta_z) & \cos(\theta_x) & 0 \\ 0 & 0 & 1 \end{bmatrix} \tag{1.4c}$$

Sometimes, it is useful to express a rotation as a combination of three rotations described by $\boldsymbol{R}_x$, $\boldsymbol{R}_y$ and $\boldsymbol{R}_z$. The order of rotation is very important[7], therefore, in this study, rotations are expressed as three successive rotations about the coordinate axes of the moving frame (1.5).

---

[7]Rotations are non commutative in 3D.

$$^A\boldsymbol{R}_B(\alpha, \beta, \gamma) = \boldsymbol{R}_u(\alpha)\boldsymbol{R}_v(\beta)\boldsymbol{R}_c(\gamma) \tag{1.5}$$

Such rotation can be parameterized by three Euler angles (α, β, γ), which can be computed from a given rotation matrix using equations (1.6).

$$\alpha = \text{atan2}(-R_{23}/\cos(\beta),\ R_{33}/\cos(\beta)) \tag{1.6a}$$

$$\beta = \text{atan2}(R_{13},\ \sqrt{R_{11}^2 + R_{12}^2}) \tag{1.6b}$$

$$\gamma = \text{atan2}(-R_{12}/\cos(\beta),\ R_{11}/\cos(\beta)) \tag{1.6c}$$

Motion of a Rigid Body   Since the relative positions of a rigid body with respect to a moving frame $\{B\}$ attached to it are fixed for all time, it is sufficient to know the position of the origin of the frame O_B and the orientation of the frame $\{B\}$ with respect to the fixed frame $\{A\}$, to represent the position of any point P in the space.

Therefore, the pose of a rigid body can be fully determined by:

1. The position vector of point O_B with respect to frame $\{A\}$ which is denoted $^AP_{O_B}$

2. The orientation of the rigid body, or the moving frame $\{B\}$ attached to it with respect to the fixed frame $\{A\}$, that is represented by $^A\boldsymbol{R}_B$.

The position of any point P of the rigid body with respect to the fixed frame $\{A\}$, which is denoted $^A\boldsymbol{P}$ may be determined thanks to the *Chasles' theorem*, which states that if the pose of a rigid body $\{^A\boldsymbol{R}_B, {}^AP_{O_B}\}$ is given, then the position of any point P of this rigid body with respect to $\{A\}$ is given by Equation (1.7).

$$^AP = {}^A\boldsymbol{R}_B{}^BP + {}^AP_{O_B} \tag{1.7}$$

While equation (1.7) can describe the motion of a rigid body, it can be written in a more convenient way using 4×4 homogeneous transformation matrices and 4×1 homogeneous coordinates. The homogeneous transformation matrix is composed of the rotation matrix $^A\boldsymbol{R}_B$ representing the orientation and the position vector $^AP_{O_B}$ representing the translation. It is partitioned as shown in Equation (1.8).

$$^A\boldsymbol{T}_B = \left[\begin{array}{ccc|c} & ^A\boldsymbol{R}_B & & ^AP_{O_B} \\ \hline 0 & 0 & 0 & 1 \end{array}\right] \tag{1.8}$$

Then, ^AP can be computed from ^BP and the homogeneous transformation matrix using (1.9).

$$\left[\begin{array}{c} ^AP \\ \hline 1 \end{array}\right] = \left[\begin{array}{ccc|c} & ^A\boldsymbol{R}_B & & ^AP_{O_B} \\ \hline 0 & 0 & 0 & 1 \end{array}\right]\left[\begin{array}{c} ^BP \\ \hline 1 \end{array}\right] \quad \Rightarrow \quad ^AP = {}^A\boldsymbol{R}_B{}^BP + {}^AP_{O_B} \tag{1.9}$$

One key advantage of homogeneous transformation is that it can easily be generalized for consecutive transformations. Let us consider the motion of a rigid body described at three locations (Figure 1.7). Frame $\{A\}$ represents the initial location, frame $\{B\}$ is an intermediate location, and frame $\{C\}$ represents the rigid body at its final location.
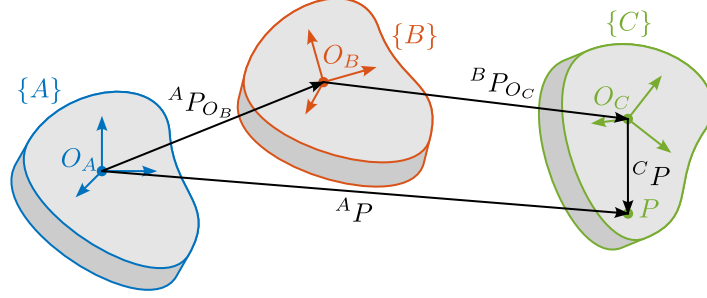

Figure 1.7: Motion of a rigid body represented at three locations by frame $\{A\}$, $\{B\}$ and $\{C\}$

Furthermore, suppose the position vector of a point P of the rigid body is given in the final location, that is ^{C}P is given, and the position of this point is to be found in the fixed frame $\{A\}$, that is ^{A}P. Since the locations of the rigid body are known relative to each other, ^{C}P can be transformed to ^{B}P using $^{B}\boldsymbol{T}_{C}$ using $^{B}P = {}^{B}\boldsymbol{T}_{C}{}^{C}P$. Similarly, ^{B}P can be transformed into ^{A}P using $^{A}P = {}^{A}\boldsymbol{T}_{B}{}^{B}P$.

Combining the two relations, Equation (1.10) is obtained. This shows that combining multiple transformations is equivalent as to compute 4×4 matrix multiplications.

$$^{A}P = \underbrace{{}^{A}\boldsymbol{T}_{B}{}^{B}\boldsymbol{T}_{C}}_{^{A}\boldsymbol{T}_{C}}{}^{C}P \tag{1.10}$$

Another key advantage of homogeneous transformation is the easy inverse transformation, which can be computed using Equation (1.11).

$$^{B}\boldsymbol{T}_{A} = {}^{A}\boldsymbol{T}_{B}^{-1} = \left[\begin{array}{ccc|c} & {}^{A}\boldsymbol{R}_{B}^{T} & & -{}^{A}\boldsymbol{R}_{B}^{T}{}^{A}P_{O_{B}} \\ \hline 0 & 0 & 0 & 1 \end{array} \right] \tag{1.11}$$

1.3 Micro-Station Kinematics

Each stage is described by two frames; one is attached to the fixed platform $\{A\}$ while the other is fixed to the mobile platform $\{B\}$. At "rest" position, the two have the same pose and coincide with the point of interest ($O_A = O_B$). An example of the tilt stage is shown in Figure 1.8. The mobile frame of the translation stage is equal to the fixed frame of the tilt stage: $\{B_{D_y}\} = \{A_{R_y}\}$. Similarly, the mobile frame of the tilt stage is equal to the fixed frame of the spindle: $\{B_{R_y}\} = \{A_{R_z}\}$.

The motion induced by a positioning stage can be described by a homogeneous transformation matrix from frame $\{A\}$ to frame $\{B\}$ as explain in Section 1.3. As any motion stage induces parasitic motion in all 6 DoF, the transformation matrix representing its induced motion can be written as in (1.12).
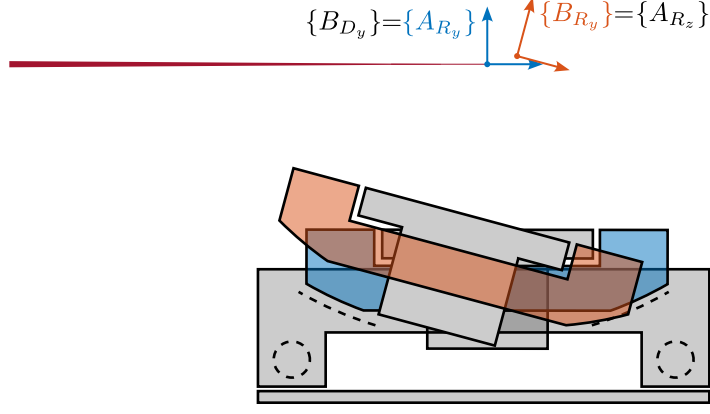
Figure 1.8: Example of the motion induced by the tilt-stage R_y. "Rest" position in shown in blue while a arbitrary position in shown in red. Parasitic motions are here magnified for clarity.

$$
{}^A\boldsymbol{T}_B(D_x, D_y, D_z, \theta_x, \theta_y, \theta_z) =
\left[
\begin{array}{ccc|c}
 & & & D_x \\
 & \boldsymbol{R}_x(\theta_x)\boldsymbol{R}_y(\theta_y)\boldsymbol{R}_z(\theta_z) & & D_y \\
 & & & D_z \\
\hline
0 & 0 & 0 & 1
\end{array}
\right]
\tag{1.12}
$$

The homogeneous transformation matrix corresponding to the micro-station $\boldsymbol{T}_{\mu\text{-station}}$ is simply equal to the matrix multiplication of the homogeneous transformation matrices of the individual stages as shown in Equation (1.13).

$$
\boldsymbol{T}_{\mu\text{-station}} = \boldsymbol{T}_{D_y} \cdot \boldsymbol{T}_{R_y} \cdot \boldsymbol{T}_{R_z} \cdot \boldsymbol{T}_{\mu\text{-hexapod}}
\tag{1.13}
$$

$\boldsymbol{T}_{\mu\text{-station}}$ represents the pose of the sample (supposed to be rigidly fixed on top of the positioning-hexapod) with respect to the granite.

If the transformation matrices of the individual stages are each representing a perfect motion (i.e. the stages are supposed to have no parasitic motion), $\boldsymbol{T}_{\mu\text{-station}}$ then represent the pose setpoint of the sample with respect to the granite. The transformation matrices for the translation stage, tilt stage, spindle, and positioning hexapod can be written as shown in Equation (1.14).

$$
\begin{aligned}
\boldsymbol{T}_{D_y} &=
\begin{bmatrix}
1 & 0 & 0 & 0 \\
0 & 1 & 0 & D_y \\
0 & 0 & 1 & 0 \\
0 & 0 & 0 & 1
\end{bmatrix}
&
\boldsymbol{T}_{\mu\text{-hexapod}} &=
\left[
\begin{array}{ccc|c}
 & & & D_{\mu x} \\
 & \boldsymbol{R}_x(\theta_{\mu x})\boldsymbol{R}_y(\theta_{\mu y})\boldsymbol{R}_z(\theta_{\mu z}) & & D_{\mu y} \\
 & & & D_{\mu z} \\
\hline
0 & 0 & 0 & 1
\end{array}
\right]
\\[2mm]
\boldsymbol{T}_{R_z} &=
\begin{bmatrix}
\cos(\theta_z) & -\sin(\theta_z) & 0 & 0 \\
\sin(\theta_z) & \cos(\theta_z) & 0 & 0 \\
0 & 0 & 1 & 0 \\
0 & 0 & 0 & 1
\end{bmatrix}
&
\boldsymbol{T}_{R_y} &=
\begin{bmatrix}
\cos(\theta_y) & 0 & \sin(\theta_y) & 0 \\
0 & 1 & 0 & 0 \\
-\sin(\theta_y) & 0 & \cos(\theta_y) & 0 \\
0 & 0 & 0 & 1
\end{bmatrix}
\end{aligned}
\tag{1.14}
$$

2 Micro-Station Dynamics

In this section, the multi-body model of the micro-station is presented. Such model consists of several rigid bodies connected by springs and dampers. The inertia of the solid bodies and the stiffness properties of the guiding mechanisms were first estimated based on the CAD model and data-sheets (Section 2.1).

The obtained dynamics is then compared with the modal analysis performed on the micro-station (Section 2.2).

As the dynamics of the nano-hexapod is impacted by the micro-station compliance, the most important dynamical characteristic that should be well modeled is the overall compliance of the micro-station. To do so, the 6-DoF compliance of the micro-station is measured and then compared with the 6-DoF compliance extracted from the multi-body model (Section 2.3).

2.1 Multi-Body Model

By performing a modal analysis of the micro-station, it was verified that in the frequency range of interest, each stage behaved as a rigid body. This confirms that a multi-body model can be used to properly model the micro-station.

A multi-body model consists of several solid bodies connected by joints. Each solid body can be represented by its inertia properties (most of the time computed automatically from the 3D model and material density). Joints are used to impose kinematic constraints between solid bodies and to specify dynamical properties (i.e. spring stiffness and damping coefficient). External forces can be used to model disturbances, and "sensors" can be used to measure the relative pose between two defined frames.
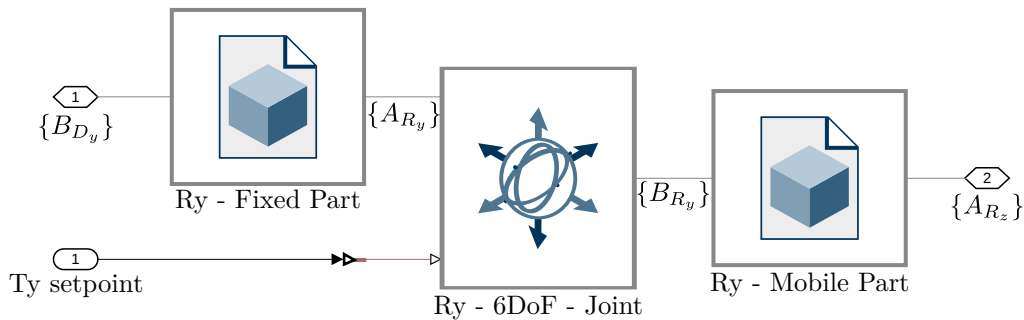

Figure 2.1: Example of a stage (here the tilt-stage) represented in the multi-body model software (Simscape). It is composed of two solid bodies connected by a 6-DoF joint. One joint DoF (here the tilt angle) can be imposed, the other DoFs are represented by springs and dampers. Additional disturbances forces for all DoF can be included

11

Therefore, the micro-station is modeled by several solid bodies connected by joints. A typical stage (here the tilt-stage) is modeled as shown in Figure 2.1 where two solid bodies (the fixed part and the mobile part) are connected by a 6-DoF joint. One DoF of the 6-DoF joint is "imposed" by a setpoint (i.e. modeled as infinitely stiff), while the other 5 are each modeled by a spring and damper. Additional forces can be used to model disturbances induced by the stage motion. The obtained 3D representation of the multi-body model is shown in Figure 2.2.
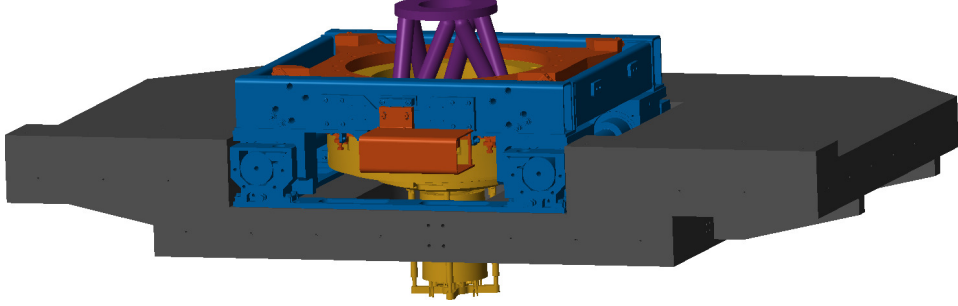

Figure 2.2: 3D view of the micro-station multi-body model

The ground is modeled by a solid body connected to the "world frame" through a joint only allowing 3 translations. The granite was then connected to the ground using a 6-DoF joint. The translation stage is connected to the granite by a 6-DoF joint, but the D_y motion is imposed. Similarly, the tilt-stage and the spindle are connected to the stage below using a 6-DoF joint, with 1 imposed DoF each time. Finally, the positioning hexapod has 6-DoF.

The total number of "free" degrees of freedom is 27, so the model has 54 states. The springs and dampers values were first estimated from the joint/stage specifications and were later fined-tuned based on the measurements. The spring values are summarized in Table 2.1.

Stage	D_x	D_y	D_z	R_x	R_y	R_z
Granite	$5\,kN/\mu m$	$5\,kN/\mu m$	$5\,kN/\mu m$	$25\,Nm/\mu\mathrm{rad}$	$25\,Nm/\mu\mathrm{rad}$	$10\,Nm/\mu\mathrm{rad}$
Translation	$200\,N/\mu m$	-	$200\,N/\mu m$	$60\,Nm/\mu\mathrm{rad}$	$90\,Nm/\mu\mathrm{rad}$	$60\,Nm/\mu\mathrm{rad}$
Tilt	$380\,N/\mu m$	$400\,N/\mu m$	$380\,N/\mu m$	$120\,Nm/\mu\mathrm{rad}$	-	$120\,Nm/\mu\mathrm{rad}$
Spindle	$700\,N/\mu m$	$700\,N/\mu m$	$2\,kN/\mu m$	$10\,Nm/\mu\mathrm{rad}$	$10\,Nm/\mu\mathrm{rad}$	-
Hexapod	$10\,N/\mu m$	$10\,N/\mu m$	$100\,N/\mu m$	$1.5\,Nm/rad$	$1.5\,Nm/rad$	$0.27\,Nm/rad$

Table 2.1: Summary of the stage stiffnesses. The contrained degrees-of-freedom are indicated by "-". The frames in which the 6-DoF joints are defined are indicated in figures found in Section 1.1

2.2 Comparison with the measured dynamics

The dynamics of the micro-station was measured by placing accelerometers on each stage and by impacting the translation stage with an instrumented hammer in three directions. The obtained FRFs were then projected at the CoM of each stage.

To gain a first insight into the accuracy of the obtained model, the FRFs from the hammer impacts to the acceleration of each stage were extracted from the multi-body model and compared with the measurements in Figure 2.3.

Even though there is some similarity between the model and the measurements (similar overall shapes and amplitudes), it is clear that the multi-body model does not accurately represent the complex micro-station dynamics. Tuning the numerous model parameters to better match the measurements is a highly non-linear optimization problem that is difficult to solve in practice.
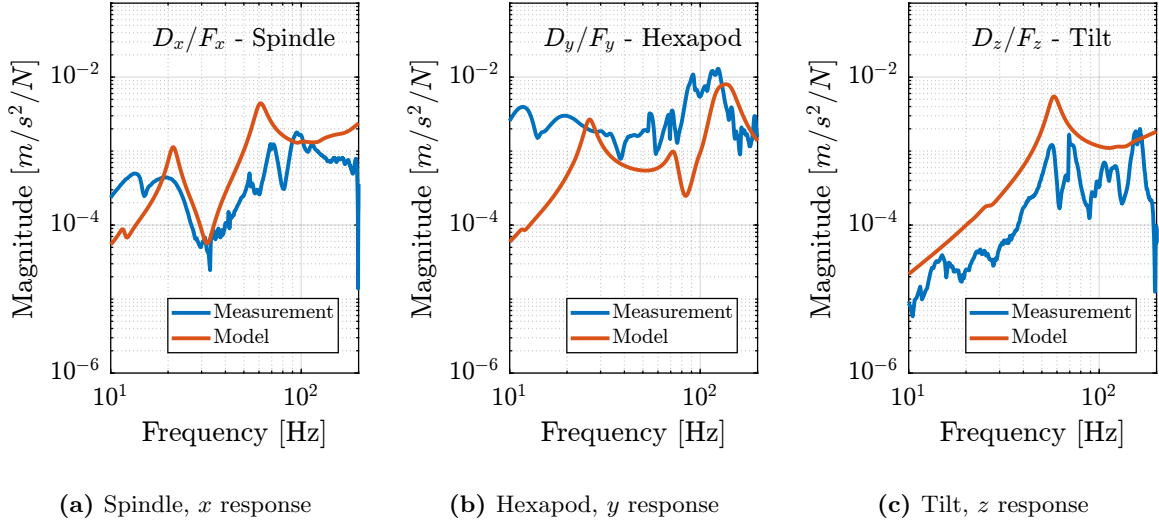

(a) Spindle, x response   **(b)** Hexapod, y response   **(c)** Tilt, z response

Figure 2.3: FRFs between the hammer impacts on the translation stage and the measured stage acceleration expressed at its CoM. Comparison of the measured and extracted FRFs from the multi-body model. Different directions are computed for different stages.

2.3 Micro-station compliance

As discussed in the previous section, the dynamics of the micro-station is complex, and tuning the multi-body model parameters to obtain a perfect match is difficult.

When considering the NASS, the most important dynamical characteristics of the micro-station is its compliance, as it can affect the plant dynamics. Therefore, the adopted strategy is to accurately model the micro-station compliance.

The micro-station compliance was experimentally measured using the setup illustrated in Figure 2.4. Four 3-axis accelerometers were fixed to the micro-hexapod top platform. The micro-hexapod top platform was impacted at 10 different points. For each impact position, 10 impacts were performed to average and improve the data quality.

To convert the 12 acceleration signals $a_{\mathcal{L}} = [a_{1x} \; a_{1y} \; a_{1z} \; a_{2x} \; \ldots \; a_{4z}]$ to the acceleration expressed in the frame $\{\mathcal{X}\}$ $a_{\mathcal{X}} = [a_{dx} \; a_{dy} \; a_{dz} \; a_{rx} \; a_{ry} \; a_{rz}]$, a Jacobian matrix $\boldsymbol{J}_a$ is written based on the positions and orientations of the accelerometers (2.1).
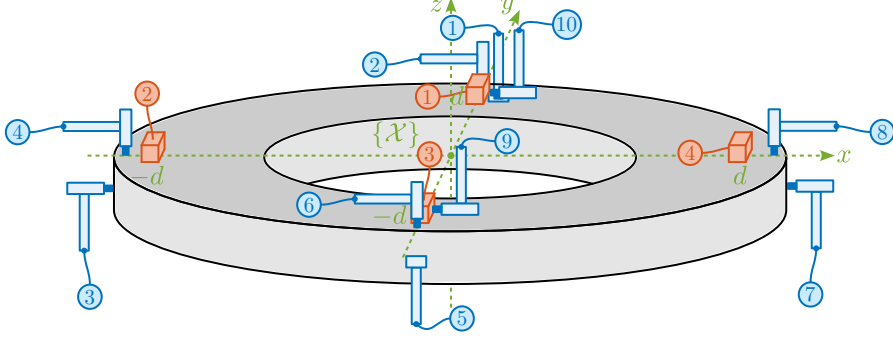
Figure 2.4: Schematic of the measurement setup used to estimate the compliance of the micro-station. The top platform of the positioning hexapod is shown with four 3-axis accelerometers (shown in red) are on top. 10 hammer impacts are performed at different locations (shown in blue).

$$
\boldsymbol{J}_a =
\begin{bmatrix}
1 & 0 & 0 & 0 & 0 & -d \\
0 & 1 & 0 & 0 & 0 & 0 \\
0 & 0 & 1 & d & 0 & 0 \\
1 & 0 & 0 & 0 & 0 & 0 \\
0 & 1 & 0 & 0 & 0 & -d \\
0 & 0 & 1 & 0 & d & 0 \\
1 & 0 & 0 & 0 & 0 & d \\
0 & 1 & 0 & 0 & 0 & 0 \\
0 & 0 & 1 & -d & 0 & 0 \\
1 & 0 & 0 & 0 & 0 & 0 \\
0 & 1 & 0 & 0 & 0 & d \\
0 & 0 & 1 & 0 & -d & 0
\end{bmatrix}
\tag{2.1}
$$

Then, the acceleration in the cartesian frame can be computed using (2.2).

$$
a_\mathcal{X} = \boldsymbol{J}_a^\dagger \cdot a_\mathcal{L}
\tag{2.2}
$$

Similar to what is done for the accelerometers, a Jacobian matrix $\boldsymbol{J}_F$ is computed (2.3) and used to convert the individual hammer forces $F_\mathcal{L}$ to force and torques $F_\mathcal{X}$ applied at the center of the micro-hexapod top plate (defined by frame $\{\mathcal{X}\}$ in Figure 2.4).

$$
\boldsymbol{J}_F =
\begin{bmatrix}
0 & -1 & 0 & 0 & 0 & 0 \\
0 & 0 & -1 & -d & 0 & 0 \\
1 & 0 & 0 & 0 & 0 & 0 \\
0 & 0 & -1 & 0 & -d & 0 \\
0 & 1 & 0 & 0 & 0 & 0 \\
0 & 0 & -1 & d & 0 & 0 \\
-1 & 0 & 0 & 0 & 0 & 0 \\
0 & 0 & -1 & 0 & d & 0 \\
-1 & 0 & 0 & 0 & 0 & -d \\
-1 & 0 & 0 & 0 & 0 & d
\end{bmatrix}
\tag{2.3}
$$

14

The equivalent forces and torques applied at center of $\{\mathcal{X}\}$ are then computed using (2.4).

$$F_{\mathcal{X}} = \boldsymbol{J}_F^t \cdot F_{\mathcal{L}} \qquad (2.4)$$

Using the two Jacobian matrices, the FRF from the 10 hammer impacts to the 12 accelerometer outputs can be converted to the FRF from 6 forces/torques applied at the origin of frame $\{\mathcal{X}\}$ to the 6 linear/angular accelerations of the top platform expressed with respect to $\{\mathcal{X}\}$. These FRFs were then used for comparison with the multi-body model.

The compliance of the micro-station multi-body model was extracted by computing the transfer function from forces/torques applied on the hexapod's top platform to the "absolute" motion of the top platform. These results are compared with the measurements in Figure 2.5. Considering the complexity of the micro-station compliance dynamics, the model compliance matches sufficiently well for the current application.
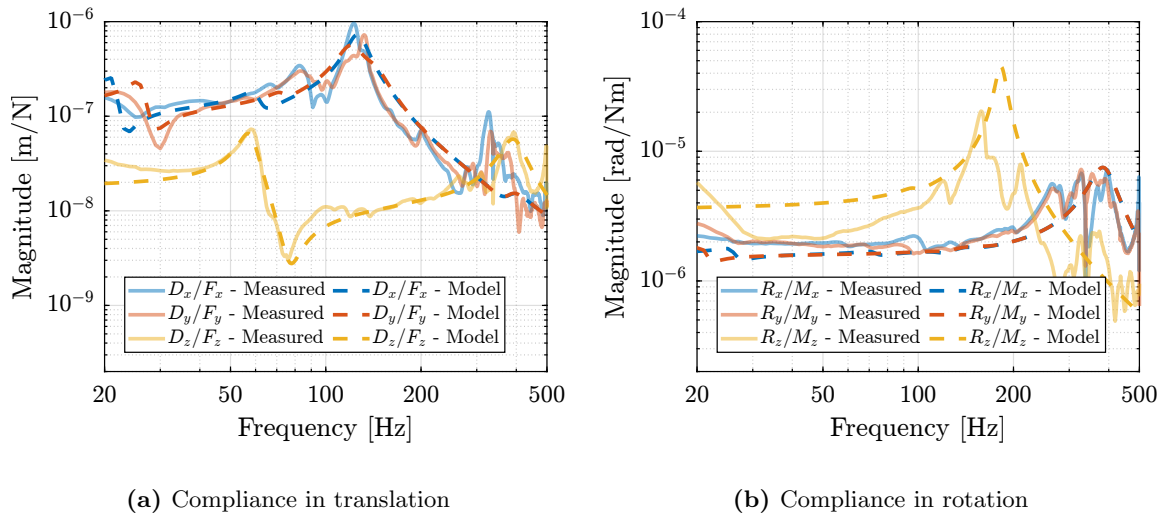

(a) Compliance in translation

(b) Compliance in rotation

Figure 2.5: Compliance of the micro-station expressed in frame $\{\mathcal{X}\}$. The measured FRFs are display by solid lines, while the FRFs extracted from the multi-body models are shown by dashed lines. Both translation terms (a) and rotational terms (b) are displayed.

3 Estimation of Disturbances

The goal of this section is to obtain a realistic representation of disturbances affecting the micro-station. These disturbance sources are then used during time domain simulations to accurately model the micro-station behavior. The focus on stochastic disturbances because, in principle, it is possible to calibrate the repeatable part of disturbances. Such disturbances include ground motions and vibrations induces by scanning the translation stage and the spindle.

In the multi-body model, stage vibrations are modeled as internal forces applied in the stage joint. In practice, disturbance forces cannot be directly measured. Instead, the vibrations of the micro-station's top platform induced by the disturbances were measured (Section 3.1).

To estimate the equivalent disturbance force that induces such vibration, the transfer functions from disturbance sources (i.e. forces applied in the stages' joint) to the displacements of the micro-station's top platform with respect to the granite are extracted from the multi-body model (Section 3.2). Finally, the obtained disturbance sources are compared in Section 3.3.

3.1 Disturbance measurements

In this section, ground motion is directly measured using geophones. Vibrations induced by scanning the translation stage and the spindle are also measured using dedicated setups.

The tilt stage and the micro-hexapod also have positioning errors; however, they are not modeled here because these two stages are only used for pre-positioning and not for scanning. Therefore, from a control perspective, they are not important.

Ground Motion The ground motion was measured by using a sensitive 3-axis geophone[1] placed on the ground. The generated voltages were recorded with a high resolution DAC, and converted to displacement using the Geophone sensitivity transfer function. The obtained ground motion displacement is shown in Figure 3.1.
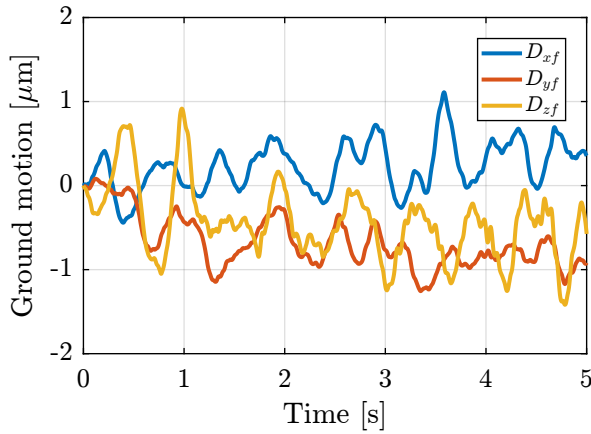
---

[1] A 3-Axis L4C geophone manufactured Sercel was used.

Figure 3.1: Measured ground motion

Figure 3.2: (3D) L-4C geophone

Ty Stage   To measure the positioning errors of the translation stage, the setup shown in Figure 3.3 is used. A special optical element (called a "straightness interferometer"[2]) is fixed on top of the micro-station, while a laser source[3] and a straightness reflector are fixed on the ground. A similar setup was used to measure the horizontal deviation (i.e. in the x direction), as well as the pitch and yaw errors of the translation stage.
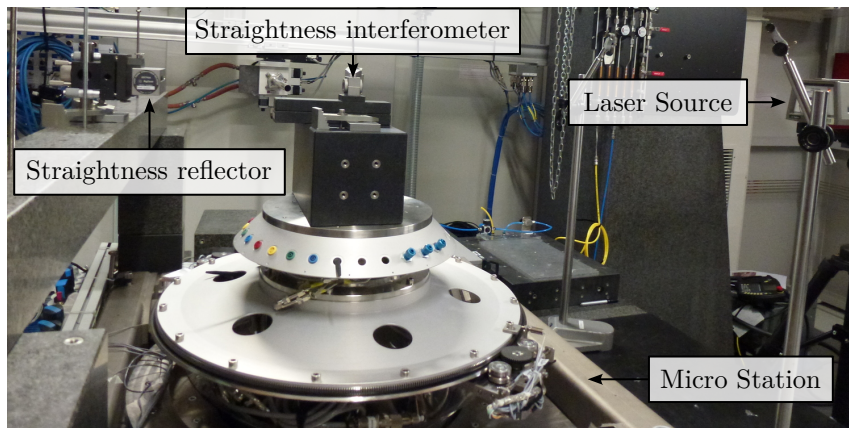

Figure 3.3: Experimental setup to measure the flatness (vertical deviation) of the translation stage

Six scans were performed between $-4.5\,mm$ and $4.5\,mm$. The results for each individual scan are shown in Figure 3.4a. The measurement axis may not be perfectly aligned with the translation stage axis; this, a linear fit is removed from the measurement. The remaining vertical displacement is shown in Figure 3.4b. A vertical error of $\pm300\,nm$ induced by the translation stage is expected. Similar result is obtained for the x lateral direction.

Spindle   To measure the positioning errors induced by the Spindle, a "Spindle error analyzer"[4] is used as shown in Figure 3.5. A specific target is fixed on top of the micro-station, which consists of two sphere

---

[2]The special optics (straightness interferometer and reflector) are manufactured by Agilent (10774A).
[3]Laser source is manufactured by Agilent (5519b).
[4]The Spindle Error Analyzer is made by Lion Precision.

(a) Measured vertical error

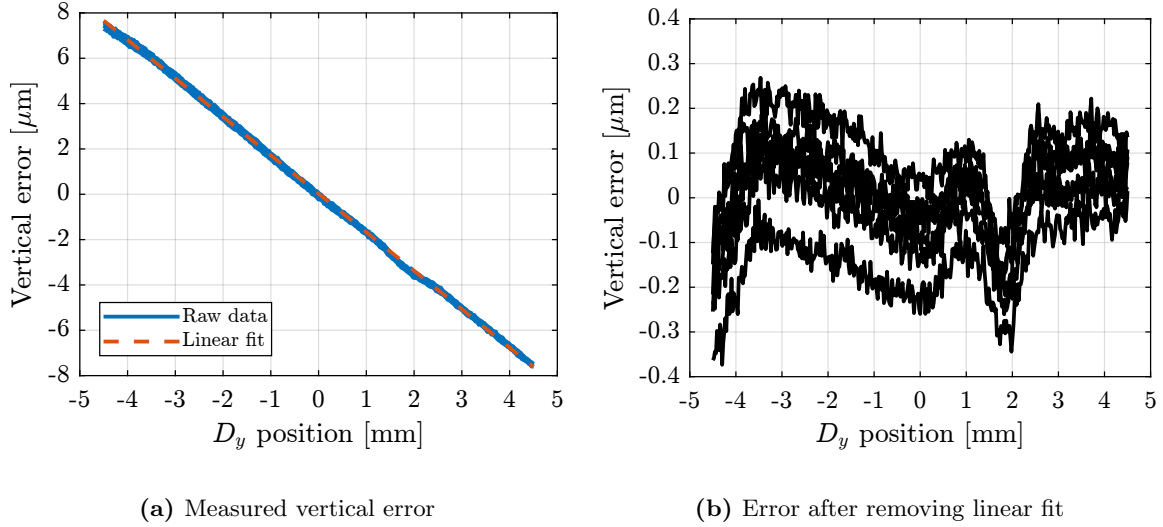**(b)** Error after removing linear fit

Figure 3.4: Measurement of the linear (vertical) deviation of the Translation stage (a). A linear fit is then removed from the data (b).

with 1 inch diameter precisely aligned with the spindle rotation axis. Five capacitive sensors[5] are pointing at the two spheres, as shown in Figure 3.5b. From the 5 measured displacements $[d_1, d_2, d_3, d_4, d_5]$, the translations and rotations $[D_x, D_y, D_z, R_x, R_y]$ of the target can be estimated.

A measurement was performed during a constant rotational velocity of the spindle of 60rpm and during 10 turns. The obtained results are shown in Figure 3.6. A large fraction of the radial (Figure 3.6a) and tilt (Figure 3.6c) errors is linked to the fact that the two spheres are not perfectly aligned with the rotation axis of the Spindle. This is displayed by the dashed circle. After removing the best circular fit from the data, the vibrations induced by the Spindle may be viewed as stochastic disturbances. However, some misalignment between the "point-of-interest" of the sample and the rotation axis will be considered because the alignment is not perfect in practice. The vertical motion induced by scanning the spindle is in the order of $\pm 30\,nm$ (Figure 3.6b).

3.2 Sensitivity to disturbances

To compute the disturbance source (i.e. forces) that induced the measured vibrations in Section 3.1, the transfer function from the disturbance sources to the stage vibration (i.e. the "sensitivity to disturbances") needs to be estimated. This is achieved using the multi-body model presented in Section 2. The obtained transfer functions are shown in Figure 3.7.
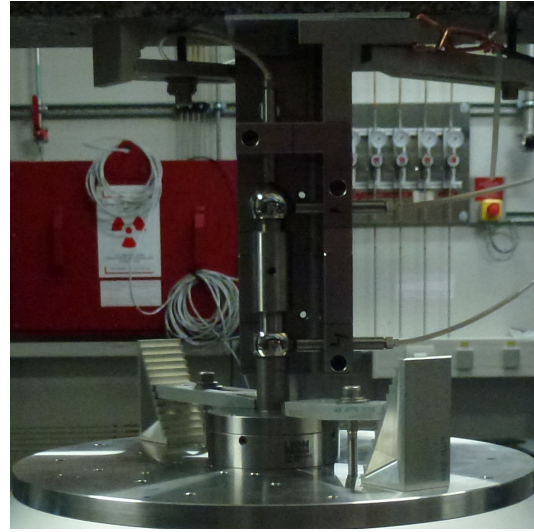
3.3 Obtained disturbance sources

From the measured effect of disturbances in Section 3.1 and the sensitivity to disturbances extracted from the multi-body model in Section 3.2, the power spectral density of the disturbance sources (i.e.

---

[5]C8 capacitive sensors and CPL290 capacitive driver electronics from Lion Precision.
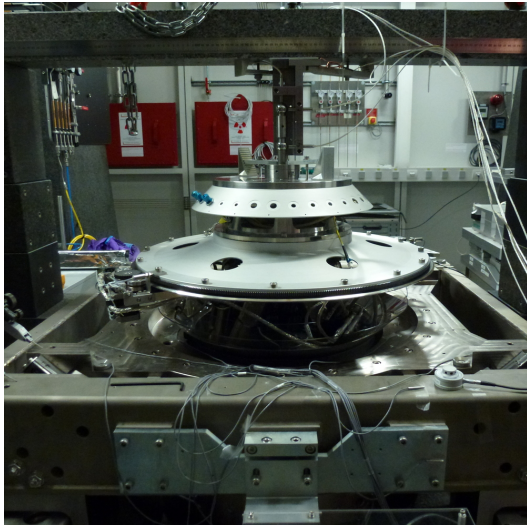
(a) Micro-station and 5-DoF metrology

(b) Zoom on the metrology system

Figure 3.5: Experimental setup used to estimate the errors induced by the Spindle rotation (a). The motion of the two reference spheres is measured using 5 capacitive sensors (b)
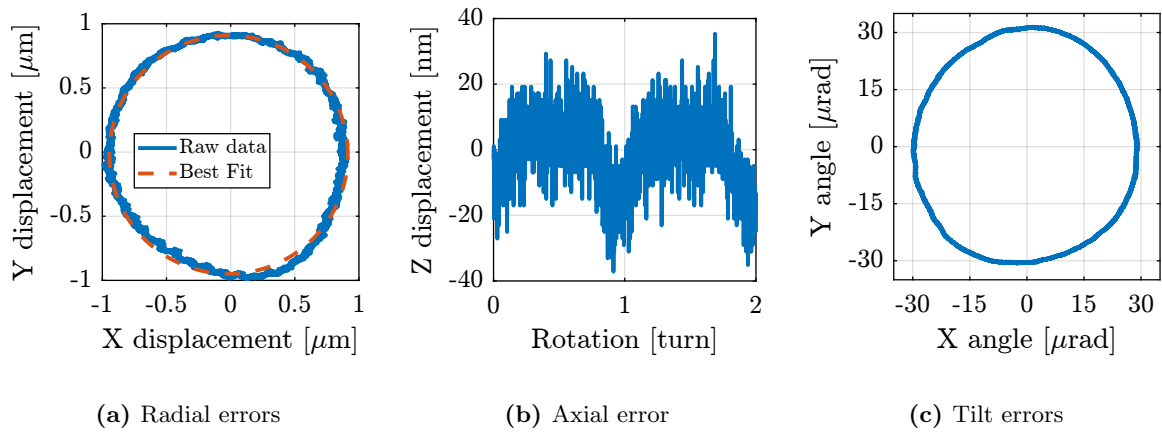

(a) Radial errors

(b) Axial error

(c) Tilt errors

Figure 3.6: Measurement of the radial (a), axial (b) and tilt (c) Spindle errors during a 60rpm spindle rotation. The circular best fit is shown by the dashed circle. It represents the misalignment of the spheres with the rotation axis.
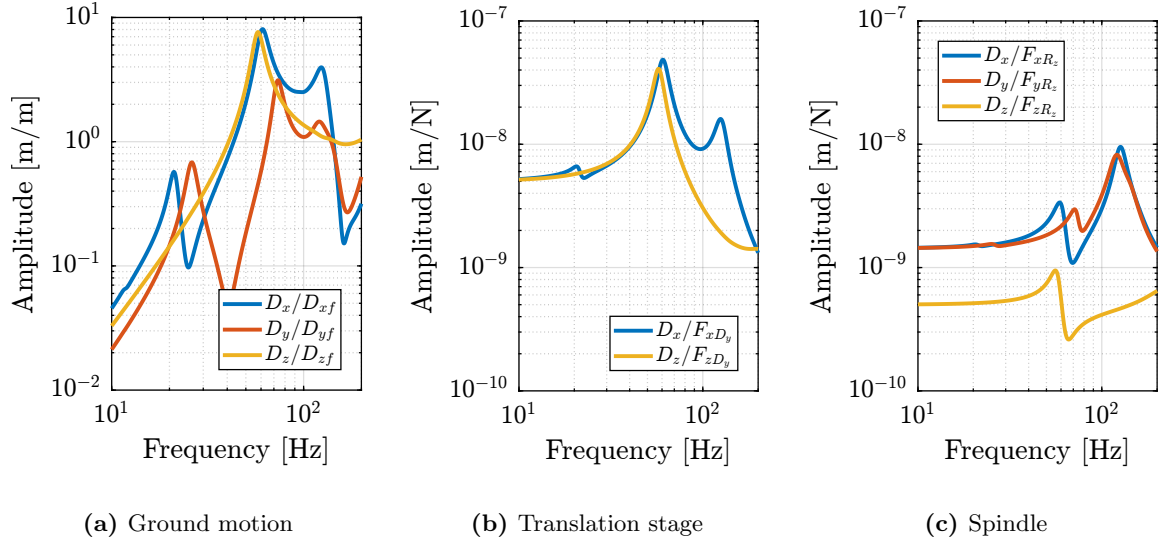
(a) Ground motion   **(b)** Translation stage   **(c)** Spindle

Figure 3.7: Extracted transfer functions from disturbances to relative motion between the micro-station's top platform and the granite. The considered disturbances are the ground motion (a), the translation stage vibrations (b), and the spindle vibrations (c).

forces applied in the stage's joint) can be estimated. The obtained power spectral density of the disturbances are shown in Figure 3.8.

The disturbances are characterized by their power spectral densities, as shown in Figure 3.8. However, to perform time domain simulations, disturbances must be represented by a time domain signal. To generate stochastic time-domain signals with a specific power spectral densities, the discrete inverse Fourier transform is used, as explained in [2, chap. 12.11]. Examples of the obtained time-domain disturbance signals are shown in Figure 3.9.
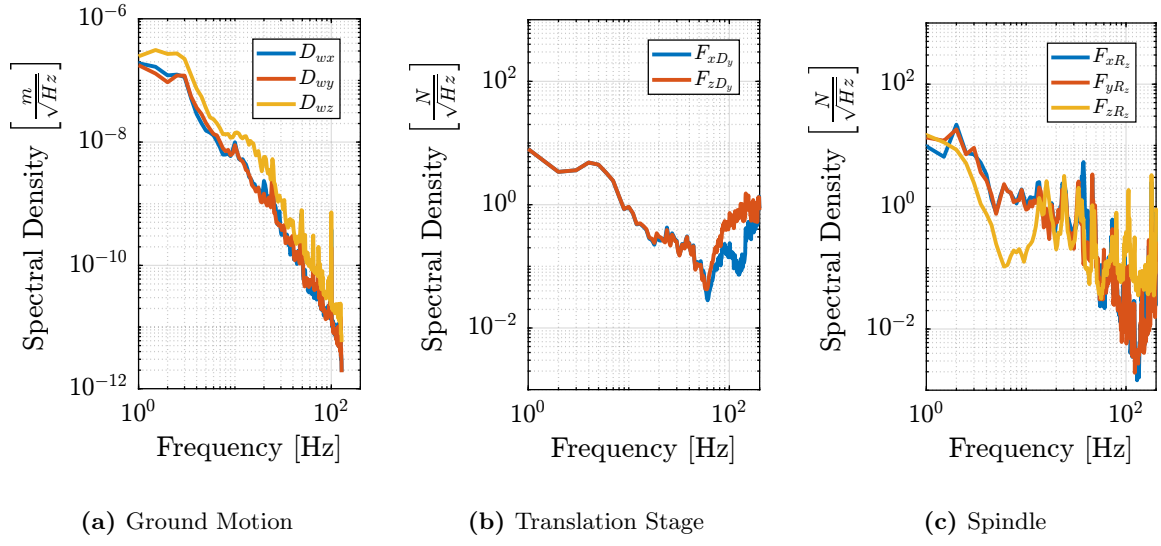
(a) Ground Motion   **(b)** Translation Stage   **(c)** Spindle

Figure 3.8: Measured spectral density of the micro-station disturbance sources. Ground motion (a), translation stage (b) and spindle (c).

(a) Ground Motion   **(b)** Translation Stage   **(c)** Spindle
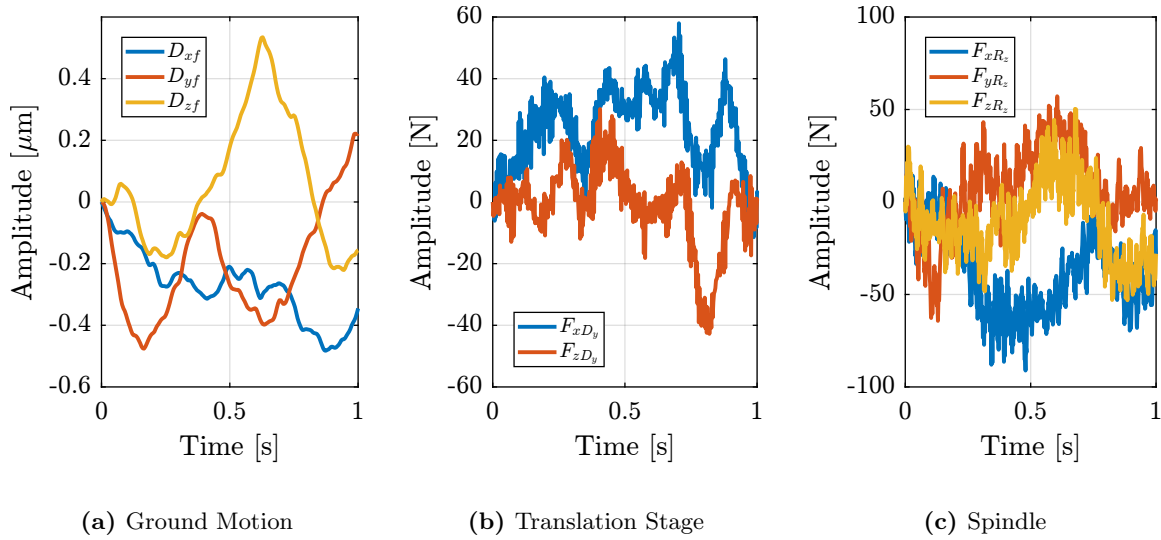
Figure 3.9: Generated time domain disturbance signals. Ground motion (a), translation stage (b) and spindle (c).

4 Simulation of Scientific Experiments

To fully validate the micro-station multi-body model, two time-domain simulations corresponding to typical use cases were performed.

First, a tomography experiment (i.e. a constant Spindle rotation) was performed and was compared with experimental measurements (Section 4.1). Second, a constant velocity scans with the translation stage was performed and also compared with the experimental data (Section 4.2).

4.1 Tomography Experiment

To simulate a tomography experiment, the setpoint of the Spindle is configured to perform a constant rotation with a rotational velocity of 60rpm. Both ground motion and spindle vibration disturbances were simulated based on what was computed in Section 3. A radial offset of $\approx 1 \, \mu m$ between the "point-of-interest" and the spindle's rotation axis is introduced to represent what is experimentally observed. During the 10 second simulation (i.e. 10 spindle turns), the position of the "point-of-interest" with respect to the granite was recorded. Results are shown in Figure 4.1. A good correlation with the measurements is observed both for radial errors (Figure 4.1a) and axial errors (Figure 4.1b).
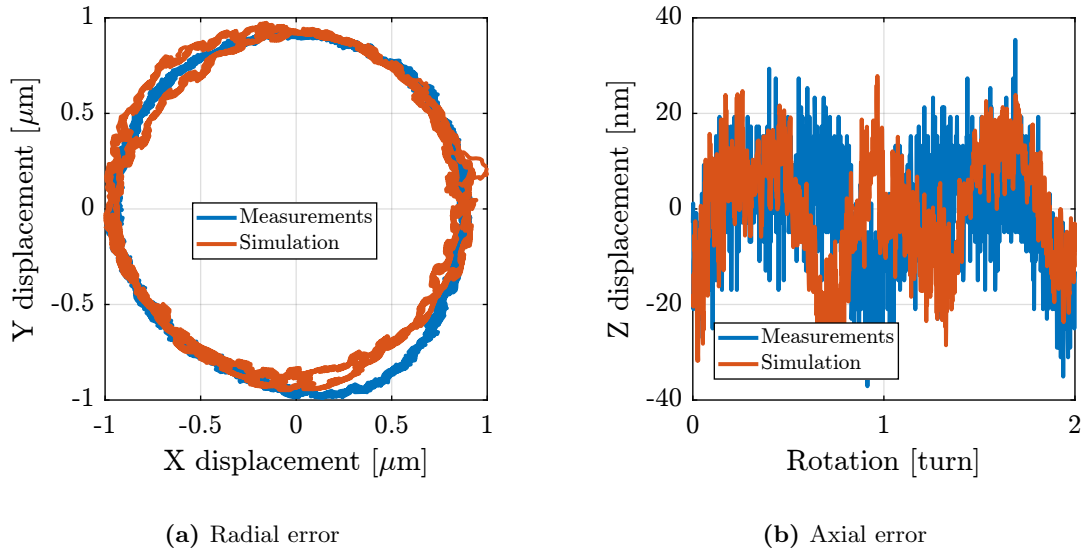

(a) Radial error

(b) Axial error

Figure 4.1: Simulation results for a tomography experiment at constant velocity of 60rpm. The comparison is made with measurements for both radial (a) and axial errors (b).

4.2 Raster Scans with the translation stage

A second experiment was performed in which the translation stage was scanned at constant velocity. The translation stage setpoint is configured to have a "triangular" shape with stroke of $\pm 4.5\,mm$. Both ground motion and translation stage vibrations were included in the simulation. Similar to what was performed for the tomography simulation, the PoI position with respect to the granite was recorded and compared with the experimental measurements in Figure 4.2. A similar error amplitude was observed, thus indicating that the multi-body model with the included disturbances accurately represented the micro-station behavior in typical scientific experiments.
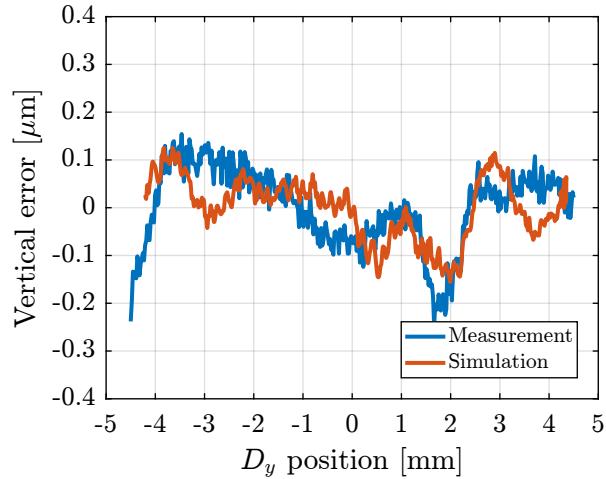

Figure 4.2: Vertical errors during a constant-velocity scan of the translation stage. Comparison of the measurements and simulated errors.

Conclusion

In this study, a multi-body model of the micro-station was developed. It was difficult to match the measured dynamics obtained from the modal analysis of the micro-station. However, the most important dynamical characteristic to be modeled is the compliance, as it affects the dynamics of the NASS. After tuning the model parameters, a good match with the measured compliance was obtained (Figure 2.5).

The disturbances affecting the sample position should also be well modeled. After experimentally estimating the disturbances (Section 3), the multi-body model was finally validated by performing a tomography simulation (Figure 4.1) as well as a simulation in which the translation stage was scanned (Figure 4.2).

Bibliography

[1] H. Taghirad, *Parallel robots : mechanics and control.* Boca Raton, FL: CRC Press, 2013 (cit. on p. 6).

[2] A. Preumont, *Random Vibration and Spectral Analysis* (Solid Mechanics and Its Applications). Springer Netherlands, 1994 (cit. on p. 20).